MnOx/IrOx as Selective Oxygen Evolution Electrocatalyst in Acidic Chloride Solution

Johannes G. Vos,[†] Tim A. Wezendonk,[‡] Adriaan W. Jeremiasse,[§] and Marc T. M. Koper*,[†]

[†]Leiden Institute of Chemistry, Leiden University, PO Box 9502, 2300 RA Leiden, The Netherlands
[‡]Delft University of Technology, Julianalaan 136, 2628 BL Delft, The Netherlands
[§]Magneto Special Anodes (an Evoqua brand), Calandstraat 109, 3125 BA Schiedam, The Netherlands

Ⓢ *Supporting Information*

ABSTRACT: The oxygen evolution reaction (OER) and chlorine evolution reaction (CER) are electrochemical processes with high relevance to water splitting for (solar) energy conversion and industrial production of commodity chemicals, respectively. Carrying out the two reactions separately is challenging, since the catalytic intermediates are linked by scaling relations. Optimizing the efficiency of OER over CER in acidic media has proven especially difficult. In this regard, we have investigated the OER versus CER selectivity of manganese oxide (MnO_x), a known OER catalyst. Thin films (~5−20 nm) of MnO_x were electrodeposited on glassy carbon-supported hydrous iridium oxide (IrO_x/GC) in aqueous chloride solutions of pH ~0.9. Using rotating ring−disk electrode voltammetry and online electrochemical mass spectrometry, it was found that deposition of MnO_x onto IrO_x decreases the CER selectivity of the system in the presence of 30 mM Cl^- from 86% to less than 7%, making it a highly OER-selective catalyst. Detailed studies of the CER mechanism and *ex-situ* structure studies using SEM, TEM, and XPS suggest that the MnO_x film is in fact not a catalytically active phase, but functions as a permeable overlayer that disfavors the transport of chloride ions.
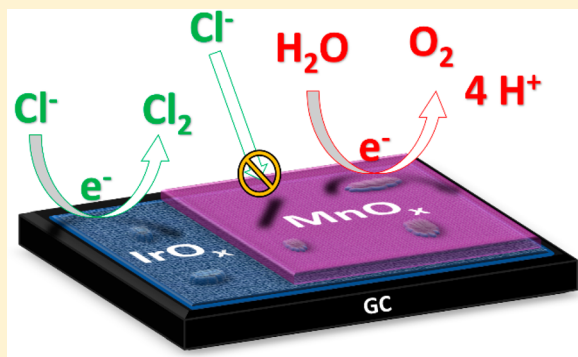
1. INTRODUCTION

A "hydrogen economy" could allow pollution-free capture and utilization of solar power as an alternative to inherently limited fossil fuels.[1] Bockris first envisioned the hydrogen economy in the 1970s as the direct electrochemical splitting of seawater into H_2 and O_2, driven by nuclear or solar power in desert areas near sea coasts, where the influx of solar energy is high and reliable.[2,3] Use of seawater would offer the benefit of having no competition with fresh water resources and could also serve as a source of very pure fresh water originating from the eventual reverse reaction in a fuel cell.[4] Despite enormous research efforts, large-scale energy storage by means of water electrolysis has not been realized yet. In large part, this is because the oxygen evolution reaction (OER), the desired anodic reaction, is inherently slow and causes major energy efficiency losses.[5−7] Bockris' original proposal raises another major challenge in saline water electrolysis, since there is the possibility of competition between OER and the oxidation of chloride ions at the anode.[8,9] The latter process manifests itself as the chlorine evolution reaction (CER) in an acidic environment, leading to the formation of Cl_2 gas. Contrary to O_2, toxic Cl_2 cannot be easily disposed of.

The competition between OER and CER is not only relevant to saline water splitting for solar energy conversion: in the energy intensive chlor-alkali process,[10,11] CER is in fact the desired reaction and OER is a detrimental side reaction.[12,13]

Metal plating and electrochemical water treatment are other examples where control over the oxidation of water or chloride plays an important role.[14,15]

On the reversible hydrogen electrode (RHE) potential scale, OER and CER proceed by

$$2H_2O \rightarrow O_2 + 4H^+ + 4e^-$$
$$E^0_{O_2/H_2O} = 1.229 \text{ V vs RHE} \tag{1}$$
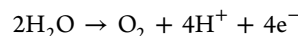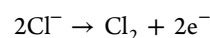
$$2Cl^- \rightarrow Cl_2 + 2e^-$$
$$E^0_{Cl_2/Cl^-} = (1.358 + 0.059pH)\text{V vs RHE} \tag{2}$$

The difficulty of catalyzing the OER lies in its four-electron nature, which implicates a reaction pathway involving a minimum of two or three intermediates.[7,16,17] It is thus inherently more complex than CER, which involves the transfer of only two electrons and presumably only a single catalytic intermediate and is therefore a much faster reaction kinetically. Although OER has a lower equilibrium potential at low pH, the kinetic advantage of CER means that Cl_2 can be the only observable product. Controlling the competition between OER and CER is not trivial, especially since it is well-

established that catalyst materials that show a proficiency toward oxidation of water also tend to catalyze the oxidation of chloride, implying that the two reactions have a similar active site or partially shared reaction pathways.[18−20] In recent computational work studying the presumed mechanisms of OER and CER, indeed a scaling relation has been observed between the binding energetics of the OER and CER intermediates, implying that catalysts that bind oxygen-bound intermediates strongly also bind chloride-bound intermediates strongly.[21−23] In a related fashion, OER is usually accompanied by catalyst degradation, a major problem for the durability of practical electrolyzers.[24−26] For pure metal oxides, the OER activity and extent of catalyst degradation during OER have been directly correlated,[25,27] implying an additional "scaling relation" between activity and degradation. However, it is also known that OER activity and catalyst degradation can be decoupled, such as by mixing with appropriate heterometal oxides.[28,29] On the other hand, CER does not seem to correlate strongly with catalyst degradation.[30−32] Unraveling the intricacies of CER versus OER selectivity is expected to lead to "cross-linked" insights in both reactions and to aid the development of better catalytic materials for both.

The majority of research concerning competition between OER and CER has been performed in light of the chlor-alkali industry, focusing on selective CER in acidic solutions on mixed metal oxides based on RuO_2 and IrO_2, stabilized by TiO_2 (so-called dimensionally stable anodes, DSAs).[33,34] Anodes that are highly OER selective in acid are very rare, due to the favorable kinetics of the CER and the OER versus CER scaling relation described above. A notable exception is manganese oxide (MnO_x), an OER-active material that has received significant interest in recent years.[35−38] Initially reported by Bennet,[39] anodes based on MnO_x show a strong tendency to selectively evolve oxygen from acidic saline water. Hashimoto et al. studied a series of Mn-based mixed metal oxides (MMO) deposited on an IrO_x/Ti substrate and showed that such anodes often exhibit nearly 100% selectivity toward OER, under a variety of experimental conditions, for many hours of sustained operation.[40−43] Besides its high reported OER selectivity, MnO_x is also one of the few nonprecious metal-based catalysts that has been reported to be moderately stable in acid under OER conditions.[44] This stability is in strong contrast with other 3d metal oxides such as CoO_x and Ni/Fe-based oxyhydroxides, materials that show very high OER activity in alkaline pH, but are unstable and inactive in acid.[6,45−50]

Inspired by Bockris' vision of a hydrogen economy based on saline water splitting plants near desert coasts, we became interested in the origin of the exceptional OER selectivity of the MnO_2-based materials studied by Hashimoto and co-workers. To our knowledge, the mechanism by which MnO_x "breaks the scaling" between OER and CER was never thoroughly investigated. In part, we believe this was due to the difficulty of reliably measuring OER versus CER activity *in situ*, for which no fast, practical method existed. We have recently developed a rotating ring−disk electrode (RRDE) method with a platinum ring electrode for chlorine detection, which allows rapid and precise CER activity measurement in acidic media.[51] Using this method, we reported CER behavior on amorphous IrO_x, a material that is considered one of the most active and stable acidic OER catalysts.[6] In the present study, we use the RRDE method to study thin films of MnO_x on IrO_x with respect to their OER and CER selectivity during cycling

voltammetry and amperometry. Product species are also studied using online electrochemical mass spectrometry (OLEMS) measurements in combination with isotopic labeling. To gain more insight in the nature of the MnO_x film, *ex-situ* studies of the catalyst were performed using bulk X-ray diffraction (XRD), scanning electron microscopy (SEM), transmission electron microscopy (TEM), and X-ray photoelectron microscopy (XPS). In this way, we aim to shed more light on the mechanism by which MnO_x-based anodes selectively evolve oxygen and how selectivity between OER and CER may be better controlled.

2. EXPERIMENTAL SECTION

All experimental protocols and details can be found in the Supporting Information.

3. RESULTS AND DISCUSSION

3.1. Deconvolution of Chlorine Evolution Rates during Parallel OER and CER by Means of an RRDE. For the quantification of CER rates during electrocatalyst operation, we make use of an RRDE setup with a Pt ring electrode, with the potential of the ring fixed at E_{Ring} = 0.95 V.[51] This enables the quantitative measurement of Cl_2 at the ring via the reduction of Cl_2 back to $Cl^−$, provided that the solution pH is below 1, to prevent hydrolysis of Cl_2 into hypochlorous acid, and the concentration of chloride is above 15 mM, to prevent interference of oxide formation on the ring.[51] Under these conditions, the collection factor for Cl_2 (N_l) was reproducible within 2% and virtually identical to that of the $Fe[CN]_6^{3−}/Fe[CN]_6^{4−}$ redox couple (N_l = 0.244; see also the Supporting Information). CER currents on the disk (i_{CER}) can then be determined by

$$i_{CER} = \left| \frac{i_{Ring}}{N_l} \right| \tag{3}$$

The main advantage of this method is its speed and flexibility in measuring CER activity during catalyst operation, which takes place on the disk electrode. Since the IrO_x/GC catalyst under study can be considered stable under the present conditions,[6] OER is the sole remaining reaction, and direct quantification of the OER current (i_{OER}) is possible via

$$i_{OER} = i_{Disk} - i_{CER} = i_{Disk} - \left| \frac{i_{Ring}}{N_l} \right| \tag{4}$$

where i_{Disk} equals the disk current, corrected for (pseudo)-capacitance by taking the average of forward and backward scans. Following the determination of i_{OER} and i_{CER}, the selectivities toward CER (ε_{CER}) and OER (ε_{OER}) are calculated from

$$\varepsilon_{CER} = 1 - \varepsilon_{OER} = \frac{1/2 i_{CER}}{1/2 i_{CER} + 1/4 i_{OER}} \tag{5}$$

Figure 1 illustrates how the RRDE method is implemented, comparing disk and ring currents for chloride concentrations of $[Cl^−]$ = 0 mM and $[Cl^−]$ = 30 mM. By observing the ring current, the onset of CER can be located at around 1.42 V, meaning it proceeds with negligible overpotential at pH = 0.88. We can then compare i_{Disk} in the absence of $Cl^−$, which is equal to "pure" OER current, and i_{OER} in the presence of 30 mM KCl, as calculated from eq 4. As was reported previously,[51] OER is not strongly affected by either the presence of $Cl^−$ or
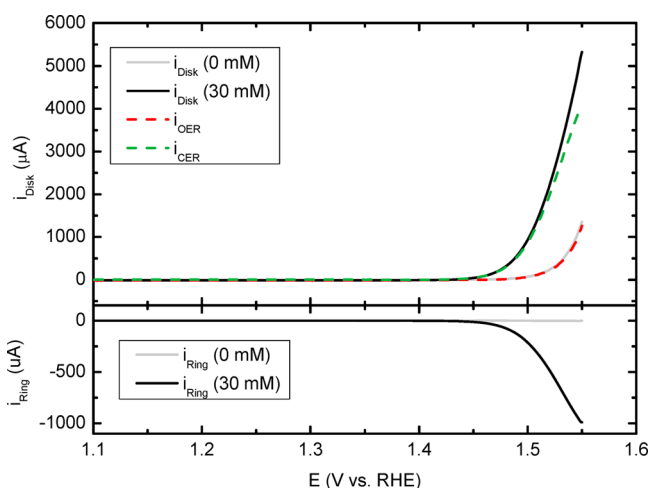
Figure 1. Representative potential scans of mixed OER and CER in 0.5 M KHSO$_4$ (pH = 0.88), to illustrate the RRDE method for aqueous Cl$_2$ detection. Top panel displays currents measured on the IrO$_x$/GC disk (i_{Disk}) in a Cl$^-$-free solution (gray curve) and in the presence of 30 mM KCl (black curve). Rotation rate: 1500 rpm. Lower panel shows corresponding currents on the Pt ring (i_{Ring}) fixed at E_{Ring} = 0.95 V. Calculation of i_{OER} and i_{CER} curves was performed using eq 3 and eq 4.

parallel CER under the used conditions. Furthermore, selectivity toward CER is approximately 86% near 1.55 V.

Although a chloride concentration of 30 mM is far removed from realistic seawater concentrations, which typically exceed 0.5 M, the use of such concentrations would compromise the ability to carry out fundamental CER studies, due to increasing experimental noise levels and interference of gas bubbles in the RRDE setup. In consideration of our previous study, where we observed no obvious changes in CER behavior for Cl$^-$ concentrations up to 100 mM,[51] we believe a concentration of 30 mM chloride constitutes an optimal system for study.

3.2. Effect of MnO$_x$ Deposition on Chlorine Evolution. In acidic media, deposition of MnO$_x$ can proceed via the overall reaction

$$2Mn^{2+} + 2H_2O \rightarrow MnO_2 + 4H^+ + 2e^-$$
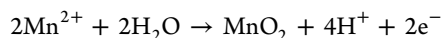
$$E^0_{MnO_x/Mn^{2+}} = (1.23 - 0.059pH) \text{ V vs RHE} \qquad (6)$$

To form MnO$_x$ films on IrO$_x$ and study their effect on CER selectivity, we resorted to growing MnO$_x$ thin films *in situ* by "spiking" the working solution with 0.6 mM MnSO$_4$. This small but significant concentration of Mn^{2+} ions prevents the net dissolution of the acid-unstable MnO$_x$ films during experiments.[44,52] Despite obvious disadvantages, such as lack of precise control over film thickness during scanning, this method allows the growth and study of thin MnO$_x$ films of variable thickness in an identical system, without the severe uncertainty of the film's integrity (and problems concerning buildup of dissolved Mn^{2+} in the solution, in the case of repeated externally grown MnO$_x$ films). It is thus possible to measure how CER kinetics depend on MnO$_x$ film growth.

Figure 2 shows CVs from 1.1−1.55 V of an IrO$_x$/GC electrode, in the presence of 30 mM KCl and 0.6 mM MnSO$_4$, under a 1500 rpm rotation rate. Compared to a Mn^{2+}-free solution, MnO$_x$ deposition manifests itself as a superimposed current with a slow onset near 1.37 V (see Figure S4 for a close-up). To grow MnO$_x$ films of variable thickness and to
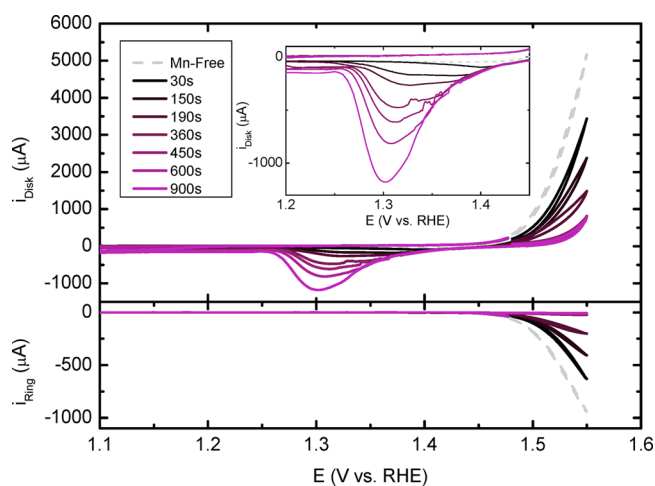

Figure 2. Top panel shows CVs of an IrO$_x$/GC rotating disk electrode (top) in 0.5 M KHSO$_4$, 30 mM KCl (pH = 0.88), and 0.6 mM MnSO$_4$ (except for the Mn^{2+}-free experiment). Rotation rate: 1500 rpm. MnO$_x$ films were preconditioned at various times at 1.48 V before initiating the forward scan at 1.48 V. The lower panel shows the corresponding i_{Ring} (E_{Ring} = 0.95 V).

test their effect on CER activity, we first conditioned the disk electrode at E_{Disk} = 1.48 V, while rotating at 1500 rpm. The conditioning potential was chosen such that it was more positive than $E^{eq}_{MnO_x/Mn^{2+}}$ (approximately 1.13 V at pH = 0.88), but not too far into the mixed OER/CER region as to prevent excessive gas formation during deposition. Immediately after conditioning, the electrode was scanned up to a positive potential limit of E = 1.55 V. At the same time, the ring was kept at E_{Ring} = 0.95 V; analogous to results described in Section 3.1, the ring is assumed to act as a selective probe for chlorine. Formation of Cl$_2$ can be seen in both the forward and reverse sweep. During the reverse scan, complete cathodic dissolution of the MnO$_x$ films appears as a reduction wave from approximately 1.450 to 1.15 V. Dissolution of the film effectively "resets" the working electrode, and the charge under the reduction peak (described as Q_{MnO_x}) allows to approximate the thickness of the film that was originally present in the forward scan. Repeated scanning without preconditioning led to overlapping CVs, with reproducible peak currents, ring currents, and cathodic MnO$_x$ dissolution peaks, showing that the original system is restored every time after traversing the negative potential limit of 1.10 V (see Figure S5). A Mn^{2+} concentration of 0.6 mM was purposefully tested as optimum: lower concentrations led to impractically long deposition times, and higher [Mn^{2+}] (>1 mM) often resulted in films that were too thick to completely dissolve after returning to 1.10 V. This was evident from a remaining brown-red glow on the electrode surface and significant but slowly subsiding negative current when the potential was kept at 1.10 V. Thicker films also occasionally led to mechanical instability in the form of brown MnO$_x$ flakes peeling off the electrode during rotation. Keeping [Mn^{2+}] as low as possible also reduced the extent of continuous (uncontrolled) MnO$_x$ deposition current during scanning and allowed a more accurate comparison of i_{OER} and i_{CER}, as will be discussed below.

Figure 3 displays the measured disk and ring currents for E_{Disk} = 1.55 V as a function of Q_{MnO_x}, the charge determined from the MnO$_x$ dissolution wave in the corresponding reverse
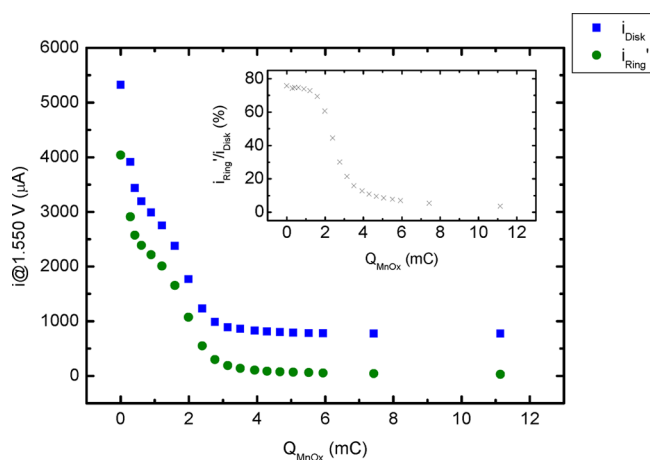
Figure 3. Disk (blue) and ring currents (green) measured at E_{Disk} = 1.55 V as a function of Q_{MnO_x}, the reductive charge measured for the corresponding MnO_x film during the backward scan, which is an approximate measure of its thickness. Inset shows the ratio between i_{Disk} and i_{Ring} corrected for N_l (i_{Ring}'). Values were determined from CVs such as those in Figure 2.

sweeps. We chose the potential of 1.55 V for quantitative analysis, since this is the point of potential reversal and as such contains minimal current contributions from (pseudo)-capacitive processes. To be able to compare directly, ring currents i_{Ring} are corrected for N_l to obtain i_{Ring}'. The distinction between i_{Ring}' and i_{CER} will be discussed shortly. The deposition of MnO_x has a profound effect on both i_{Disk} and i_{Ring}', but the most interesting aspect is the selectivity: i_{Ring}' is impacted very differently than i_{Disk}. As Q_{MnO_x} varies within 0−2 mC, a proportional decrease in both i_{Disk} and i_{Ring}' can be seen, leading to an approximately constant ratio i_{Ring}'/i_{Disk} (Figure 3, inset). For $Q_{MnO_x} > 2$ mC, the ratio i_{Ring}'/i_{Disk} shows a sudden drop. We also observe a change in shape of the MnO_x reduction wave as Q_{MnO_x} increases above 2 mC: below 2 mC, a single, broad reduction peak is observed, which transforms into two peaks for $Q_{MnO_x} > 2$ mC, with peak potentials shifting continuously more negative as the reduction charge increases (see also Figure S6 and Figure S7). The appearance of separate peaks may be due to proton diffusion becoming the limiting factor during film reductive dissolution.[53,54]

Unfortunately, the quantification of i_{OER} and i_{CER} in the presence of Mn^{2+} is obfuscated by Mn-related redox processes, in contrast to the measurements on MnO_x-free IrO_x in Section 3.1, where it was assumed that OER and CER were the sole reactions. There are two reasons for this: first, i_{Disk} after subtraction of i_{Ring}' is no longer "pure" OER current, but the sum of OER and MnO_x deposition current. Second, close inspection of the ring currents (Figure S4) suggests reduction of a species that appears at a potential slightly more negative than the onset potential of CER. We ascribe this additional current to the reduction of solution-phase Mn^{3+}.[55] This species originates from the disk and is a generally accepted intermediate during acidic MnO_x deposition.[53,54,56] Ring currents can thus no longer be ascribed solely to CER ($i_{Ring}' \neq i_{CER}$). To take these two sources of error into account, we use the following correction. The diffusion-limited current density of MnO_x deposition ($i_{MnO_x}^L$) is estimated at 140 μA using the Levich equation (see the Supporting Information).

This value serves as an "upper limit" of the MnO_x deposition current during OER and CER. Likewise, the maximum ring current originating from Mn^{3+} reduction can be estimated at 70 μA, representing an upper limit of ring current falsely attributed to CER. For $Q_{MnO_x} < 2$ mC, where $i_{Ring}' > 1800$ μA, we assume this error to be negligible, but at $Q_{MnO_x} > 4$ mC, the remaining ring current approaches 30 μA. In this regime, the ring current may not be unambiguously assigned to CER, and the real CER current could be significantly lower.

To still make an estimation of OER versus CER selectivity, we assume the worst-case scenario in terms of OER selectivity: this translates to (i) assuming that MnO_x deposits with diffusion-limited current densities at all potentials, allowing the calculation of the *minimum* OER current after ring current subtraction, and (ii) assuming that the N_l-corrected ring current i_{Ring}' originates only from CER, irrespective of Q_{MnO_x}, leading to the *maximum possible* CER current. In other words, eq 3 applies, like the case for the "blank" IrO_x catalyst: $i_{Ring}' = i_{CER}$. We thus use the following expression for i_{OER}:

$$i_{OER} = i_{Disk} - i_{CER} - i_{MnO_x}^L = i_{Disk} - i_{Ring}' - 140\ \mu A$$

$$(7)$$

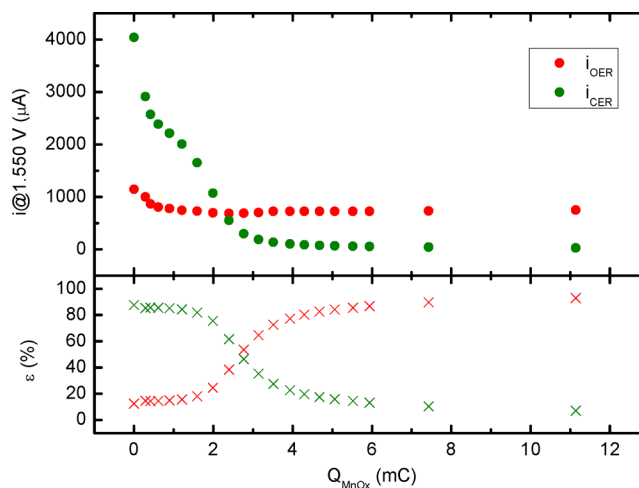**Figure 4.** Top panel: currents for OER (red) and CER (green) at E = 1.55 V, calculated from eq 3 and eq 7. Lower panel: corresponding selectivities toward OER (red) and CER (green). Data are plotted as a function of Q_{MnO_x}, the charge ascribed to the corresponding MnO_x layer, which is an approximate indication of its thickness. Values were determined from CVs such as those in Figure 2.

Figure 4 displays the calculated currents and selectivities toward OER and CER as a function of Q_{MnO_x}. As already suggested by the ratio i_{Ring}'/i_{Disk} in Figure 3, ε_{OER} rises sharply at the expense of ε_{CER} beyond a MnO_x reduction charge of 2 mC. We will refer to the reduction charge of the MnO_x film at which there is a strong shift of selectivity from CER toward OER as the "critical MnO_x charge". Figure 4 shows that modification of IrO_x by growth of a thick MnO_x film makes it >90% OER selective with a moderate (45%) drop in activity.

The dependence of CER kinetics on MnO_x deposition can be studied by making Tafel plots based on measured ring currents (Figure 5), especially at high ring currents where the
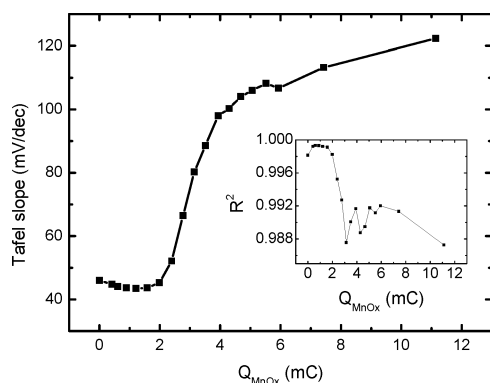
Figure 5. Tafel slopes for CER on the disk electrode, constructed from ring currents, as a function of Q_{MnO_x}. Values taken from CVs similar to Figure 2. Inset shows corresponding R^2 values (correlation coefficients), to illustrate the degree of linearity as a function of Q_{MnO_x}.

error from Mn^{3+} reduction is negligible. On "bare" IrO_x, as well as during the initial stages of MnO_x film growth ($Q_{MnO_x} < 2$ mC), CER Tafel slopes range within 40−45 mV/dec, suggesting a rate-limiting second electron transfer step controlling the CER mechanism, in correspondence with previous literature.[19,57] The Tafel curves in this regime show good linearity, as determined from R^2-values in the inset of Figure 5. As Q_{MnO_x} increases beyond the critical charge, Tafel slopes increase to ca. 120 mV/dec. This value agrees remarkably well with a mechanism where the first electron transfer step becomes rate-determining, suggesting that the apparent kinetics of the reaction change. However, a pronounced departure from linearity is also apparent (Figure 5 inset), suggesting that the measured Tafel slopes become clouded by additional effects. Above all, we expect the error from Mn^{3+} reduction to be high here, and the measured Tafel slope may well be related to the solution phase oxidation of Mn_{aq}^{2+} to Mn_{aq}^{3+} on the disk (assuming a symmetry factor α of nearly 1/2).

To gain more insight in the sudden change in CER activity, we recorded ring−disk amperometry curves to study the potential-dependent deposition behavior of MnO_x on IrO_x (Figure 6). The ring currents in the lower panel were normalized versus their initial value ($i_{Ring,t=0}$), to compare the relative decrease in CER for different potentials. An increase in E_{Disk} has a 2-fold effect: (i) i_{Disk} initially increases strongly, which is due to a rise in CER current (top panel), and (ii) CER rates start declining earlier (lower panel). It was previously postulated that MnO_x deposition proceeds through a progressive electrochemical nucleation and growth mechanism, in which the current contribution from the growth of existing nuclei is larger than current from the formation of new nuclei.[58−60] Our own findings suggest that MnO_x deposition at 1.45 V on amorphous IrO_x near pH = 1 is kinetically controlled and proceeds via a similar mechanism, since the deposition current shows an induction time followed by a peak (Figure S9). The observed drop in CER activity would then coincide with the moment where the exclusion zones of the individual MnO_x nuclei intertwine and the full coverage of the IrO_x surface by MnO_x rapidly increases.

To corroborate the RRDE findings, we measured the competition of CER versus OER on IrO_x and the effect of MnO_x deposition using OLEMS. Since the use of a stationary electrode is required in the OLEMS setup, we used a stirrer bar
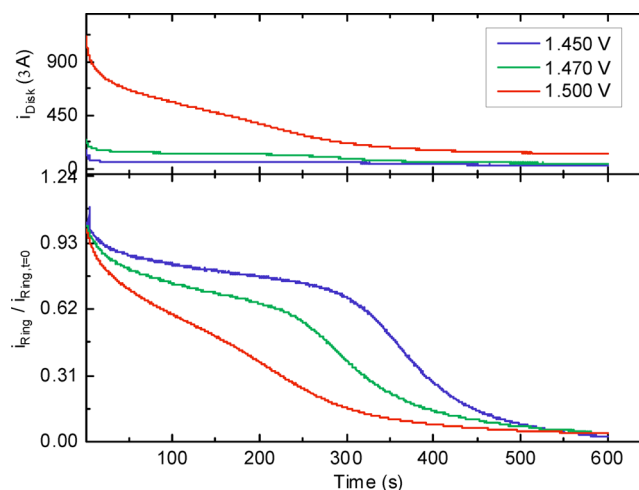

Figure 6. Top panel: amperometry measurements at increasing potentials of an IrO_x/GC rotating disk electrode (top) in 0.5 M $KHSO_4$, 20 mM KCl, and 0.6 mM $MnSO_4$ (pH = 0.87), rotation rate 1500 rpm. The lower panel shows the corresponding i_{Ring} normalized to their initial value $i_{Ring,t=0}$ ($E_{Ring} = 0.95$ V).

at ∼600 rpm to enhance mass transport of chloride and Mn^{2+} and reduce the effects of transient broadening of the diffusion layer. Despite this, mass transport to the surface was significantly lower than in the RRDE setup. To ensure a strong enough Cl_2 mass signal in the OLEMS and to reach MnO_x film growth comparable to the RRDE experiments, a relatively high concentration of chloride (80 mM) and $MnSO_4$ (1.2 mM) was used. In Figure 7A, cyclic voltammetry was performed on an IrO_x/GC electrode with a significant amount of MnO_x predeposited at 1.460 V, after which three cycles were carried out in the potential region of mixed CER, OER, and MnO_x deposition. The initial forward sweep starting from 1.460 V shows a relatively low maximum current, and the backward sweep shows a wave where the preformed MnO_x layer is reductively removed. In scans 2 and 3, the IrO_x electrode was scanned into the CER/OER region again, such that the electrode was free of preformed MnO_x. Mass signals m/z 32 and m/z 70 (corresponding to O_2^+ and Cl_2^+, ionized molecular oxygen and chlorine, respectively) were collected in the mass spectrometer during the scans. Both species have peaks in the mixed OER/CER region as expected, but there are major differences between the three cycles. The rate of Cl_2 formation is clearly suppressed during the first cycle, then strongly increases in cycles 2 and 3. The O_2 mass signal in the first scan shows significant trailing and is also higher than in scans 2 and 3. Comparison of results from scan 1 and scan 2 suggests that the emergence of CER activity is coupled to a decrease in OER activity. This appears to contradict the previous results from the RRDE method that OER and CER are independent. However, we want to note that the amount of chlorine produced in cycles 2 and 3 was rather high, which was necessary to obtain a sizable m/z 70 signal, as the majority of produced Cl_2 dissociates and recombines in the ionization chamber to form HCl^+, mass signal m/z 36.[61] It is thus highly likely that the collection efficiency of O_2 was affected by the vigorous chlorine evolution near the electrode surface. Nonetheless, we believe the most important result of the OLEMS measurements is the strong suppression of chlorine evolution in the first cycle, meaning that on an IrO_x/MnO_x electrode, O_2 is formed highly selectively.
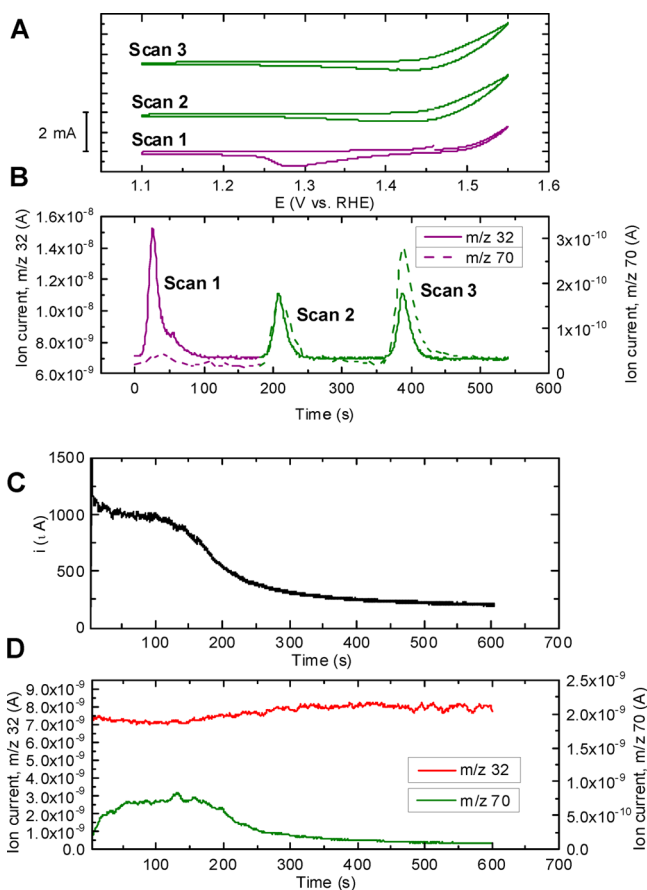
Figure 7. OLEMS measurements of an IrO_x/GC disk electrode in 0.5 M $KHSO_4$, 80 mM KCl, and 1.2 mM $MnSO_4$ (pH = 0.89). (A) CVs of the electrode after preconditioning for 450 s at 1.46 V, followed by three scans. Scan rate: 5 mV s^{-1}. (C) Amperometry at 1.500 V for 600 s. (B and D) Corresponding OLEMS mass signals over time. Solution is saturated with Ar. A stirrer bar at ~600 rpm was employed to increase mass transport.

In Figure 7C, current versus time curves were recorded at 1.50 V to investigate the effect of transient MnO_x deposition, along with changes in O_2 and Cl_2 mass signals (Figure 7D). In the current profile, the semisteady current declines abruptly after ~100 s, converging to a current of around 200 μA. The abrupt decline is reminiscent of results in Figure 6 and correlates with a selective decrease in the Cl_2 signal.

3.3. Structure of the MnO_x/IrO_x Film. The results in the previous sections show that during mixed OER and CER on an IrO_x electrode covered by a MnO_x film, there is a decrease in oxidation current coupled to strongly enhanced selectivity of

OER over CER with an increase of the coverage by the MnO_x film, as well as a change in the apparent CER Tafel slope. Besides the origin of this selectivity shift, a relevant question concerns the degree to which MnO_x is catalytically active under these conditions. OLEMS measurements on a MnO_x/GC sample in an acidic solution, without IrO_x present, showed no detectable activity for OER or CER (Figure S11), in accordance with previous literature. However, it has been reported that the crystal phase and oxide stoichiometry of MnO_x as well as the existence of metal−support interactions can greatly affect the OER performance.[62−65] We thus wanted to study the structure of the deposited materials.

For structural studies, films were grown hydrodynamically in ClO_4^- solutions in the presence of 20 mM Cl^-, allowing use of the ring electrode to monitor the rate of chlorine evolution during deposition. An amount of MnO_x was deposited such that the CER rate was approximately 50% of the initial value (Figure S12). The nature of the MnO_x films in the following studies should thus be close to films corresponding to the critical MnO_x charge of 2 mC discussed earlier. MnO_x films grown in ClO_4^- and HSO_4^- electrolytes showed identical morphologies in SEM and likewise behavior of ε_{CER} versus Q_{MnO_x}, suggesting that adsorption of HSO_4^- inhibits MnO_x deposition but does not alter its mechanism (Figure S10).

Figure 8A shows a SEM micrograph of a representative IrO_x/GC film, with a morphology corresponding well to previous reports.[66−69] The GC surface is covered by a thin layer of nanoparticulate IrO_x, as was revealed by drying-induced cracks of the film (see Figure S14B). We also occasionally observed mesoporous clusters of IrO_x particles with diameters of 50−150 nm (Figure 8B). The clusters generally occupied less than 4% of the GC electrode surface area, as estimated from SEM images of a large section of the electrode. Figure 8C and D show SEM micrographs of $MnO_x/IrO_x/GC$ samples, the films grown in the presence of 20 mM Cl^- and representing "50% CER activity": compared to MnO_x-free conditions. A porous structure of thin intertwined sheets is visible on top of the IrO_x particles and layer, which is composed of MnO_x, as verified via energy-dispersive X-ray spectroscopy (EDS) analysis. From the SEM micrographs, the MnO_x sheet thickness is within 8−10 nm (Figure S14A). MnO_x deposited on GC in the absence of IrO_x forms a similar structure (Figure S14C). The MnO_x morphologies resemble earlier SEM results of δ-MnO_2 (Birnessite), a poorly crystalline polymorph of MnO_6 octahedra arranged as sheets (see also Figure S14D for micrographs of MnO_x formed during extended deposition times).[70−73] However, we cannot draw conclusions about the MnO_x structure on the basis of SEM morphology alone.
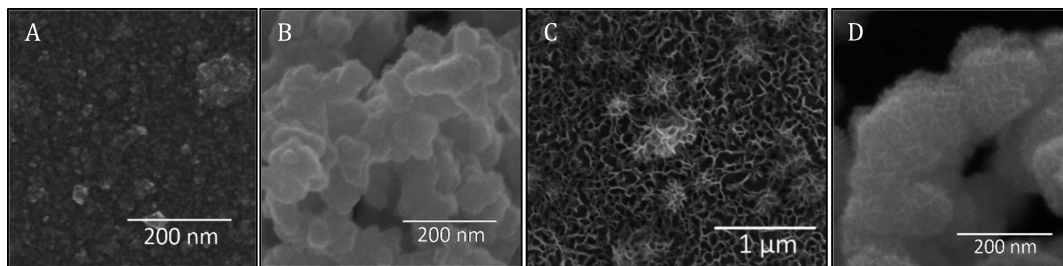

Figure 8. SEM micrographs of representative electrodes used in this study. (A and B) IrO_x/GC electrode, deposited according to the procedure described by Nakagawa et al. (C and D) $MnO_x/IrO_x/GC$ electrode; MnO_x was deposited onto IrO_x/GC as described in the text.
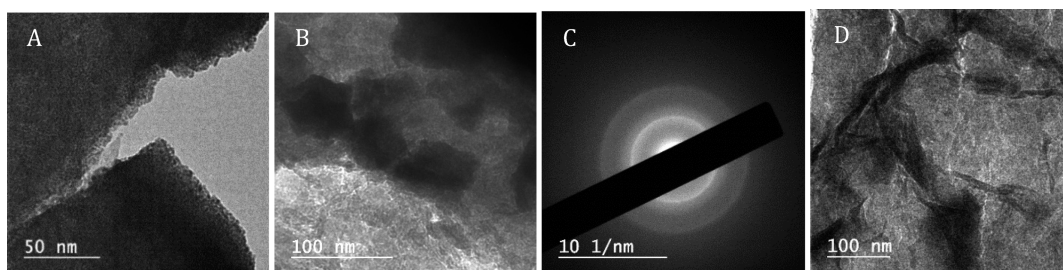
Figure 9. TEM micrographs of a MnO_x/IrO_x film that was grown identically to the films used for SEM in Figure 8, then carefully scraped off the GC support for imaging. (A) Sheets of amorphous IrO_x particles, having diameters in the range of 2−4 nm. (B) Larger IrO_x particles (diameter ∼60 nm) within the film. (C) SAED pattern of the area shown in B. Diffuse diffraction rings corresponding to rutile IrO_2 are visible. The also present MnO_x does not generate a clear contribution to the pattern. (D) Intertwined MnO_x sheets perpendicular to the beam direction, as also seen in SEM micrographs.
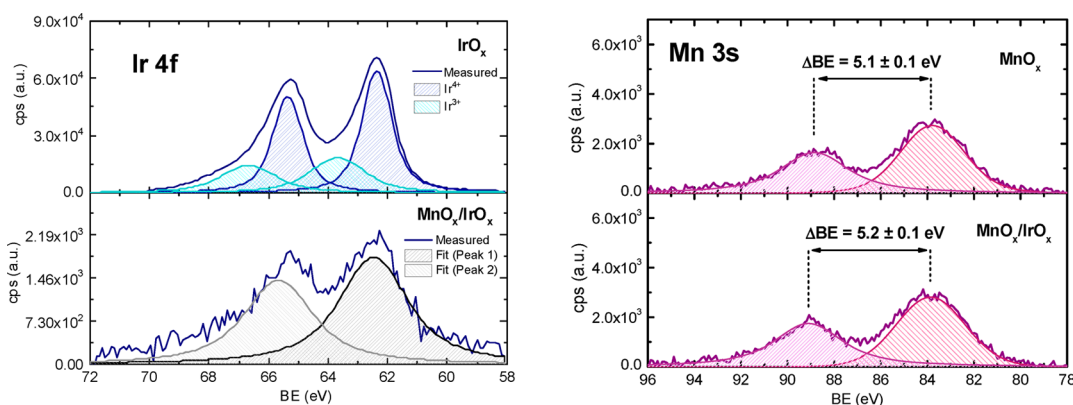

Figure 10. Core-level XPS scans of the Ir 4f (left) and Mn 3s (right) spectral peaks, on an absolute intensity scale. Both elements were scanned in samples of their MO_x/GC single oxides (top panels) and the mixed $MnO_x/IrO_x/GC$ sample (lower panels). Note the difference in scale in the lower left-hand panel, illustrating the relatively low intensity of the Ir 4f signal.

We attempted to take XRD spectra of IrO_x and the combined Mn/Ir oxide, using samples as-deposited on GC (see Figure S13). Besides the GC background, no diffraction peaks were observed, suggesting that the IrO_x and MnO_x are amorphous. Previous studies of hydrated IrO_x colloids, as well as MnO_x deposited at constant potential, also reported amorphous structures.[62,69,74,75] We must note that the films may be too thin to lead to sufficient signal in the diffractometer, although an attempt was made to compare the diffraction patterns to a small quantity of highly crystalline RuO_2. Alternatively, IrO_x nanoparticles were precipitated and isolated from acidified colloid solutions. Even when scanning such bulk samples, we could not observe XRD peaks.

To obtain more structural information on the MnO_x/IrO_x samples, we performed TEM measurements along with EDS and selected-area electron diffraction (SAED). Figure 9 shows bright-field TEM micrographs of a MnO_x/IrO_x film that was carefully scraped off the GC electrode. IrO_x nanoparticles with a diameter of 2−4 nm as well as occasionally larger particles were visible (Figure 9A and B), similar to results from Zhao et al.[66] Like the SEM results, a veiny MnO_x deposit could be seen (verified by EDS); the ∼8 nm thick sheets were visible in the microscope (Figure 9D). Despite the much higher diffraction cross-section in comparison with XRD, most SAED experiments led to diffuse patterns. We could sporadically obtain better defined radial profiles, roughly corresponding to rutile-IrO_2 (Figure 9C).[76,77] In the microscope, a rare instance of a crystallite that was also properly oriented showed a d-spacing of 3.18 Å, corresponding to the rutile IrO_2 (110) plane.[78] We

also generated SAED patterns at higher beam accelerating voltages of 200 keV (Figure S17), the result of which showed sporadic rutile-related diffractions from IrO_2 and $β$-MnO_2. Unfortunately, significant contributions from metallic Ir (and possibly Mn) were also present, likely due to beam radiation damage.[79]

To probe the electronic structure and the extent of interaction between the two oxides, we performed *ex-situ* XPS on a representative $MnO_x/IrO_x/GC$ film, as well as on single oxide reference samples termed MnO_x/GC and IrO_x/GC. Core-level Ir 4f scans were performed, as this peak is considered a reliable probe for determining the average Ir oxidation state.[78,80,81] The magnitude of the Mn 3s peak multiplet splitting serves a similar function in Mn.[82,83] Additional narrow spectra of the O 1s and Cl 2p peaks are shown in the Supporting Information (Figure S19 and Figure S20). In Figure 10, the IrO_x/GC sample has a $4f_{7/2}$ core-level binding energy of 62.4 eV, with a pronounced asymmetry indicating contributions of multiple oxidation states. The obtained binding energy is close to values reported for hydrous iridium oxides lacking long-range order.[78,84] IrO_x/GC has mainly Ir^{4+} centers, but a significant contribution of Ir^{3+} is apparent, with an estimated $Ir^{3+}:Ir^{4+}$ ratio of 0.27. The MnO_x/GC sample shows a Mn 3s peak splitting of 5.1 eV, corresponding to an average oxidation state between 3+ and 4+. The nonintegral average oxidation states of IrO_x and MnO_x suggest nonstoichiometric oxides and disordered structures, consistent with the diffraction experiments. In the $MnO_x/IrO_x/GC$ sample, Mn peaks dominate the spectral features

(Figure S18). Most of the signal originates from the MnO$_x$ overlayer, as was also verified from the appearance of a large O 1s contribution at 529.9 eV, and by comparing Mn:Ir ratios determined from XPS and amperometry deposition data (Table S1). We could nonetheless still observe the Ir 4f peak, with a peak fitting-derived binding energy of approximately 62.5 eV (see Figure 10), a shift of +0.1 eV relative to IrO$_x$/GC. The signal intensity was too weak for a more elaborate peak deconvolution. A relevant question is whether the Ir sites contributing to the weak Ir 4f peak are covered by MnO$_x$, which was suggested by the SEM measurements. The reductive charge Q$_{MnO_x}$ of grown MnO$_x$ films corresponds to a layer roughly 10 nm thick, approaching the limit for the detection depth of XPS. The weak Ir 4f peak in the sample shows a strong prevalence of inelastic scattering in the form of tailing at higher binding energies and a rise in background scattering that is disproportionately higher than the IrO$_x$/GC reference (Figure S21). We thus assume that the weak XPS Ir 4f peaks originate from subsurface Ir and that this Ir must be in intimate contact with the MnO$_x$ layer. The Mn 3s peak splitting in MnO$_x$/IrO$_x$/GC is 5.2 eV, a difference of +0.1 eV with respect to the MnO$_x$/GC reference sample. This shift may indicate a lowering of the average oxidation state,[82] but the shift is small and negligible within the margins of experimental error (±0.1 eV).

Summarizing our structural studies, we find that the formed MnO$_x$ and IrO$_x$ are amorphous and probably form non-stoichiometric oxides. The MnO$_x$ catalyst without IrO$_x$ showed no activity in OLEMS, and we could also see no evidence of a strong interaction between Mn and Ir from the almost identical Ir 4f binding energies and Mn 3s multiplet splitting in XPS. This makes it doubtful whether the close proximity of and interaction with IrO$_x$ could somehow activate MnO$_x$ for OER.

3.4. Isotopically Labeled OLEMS Measurements and OER Studies on an RDE.

Given the lack of electronic interaction between MnO$_x$ and IrO$_x$ suggested by the detailed characterization described in the previous section, we undertook isotopically labeled OLEMS measurements to further probe the origin of the OER/CER selectivity of the MnO$_x$/IrO$_x$/GC electrode. We also looked more closely into the OER behavior of the selective catalyst using RDE experiments.

In Figure 11A and B, we performed isotopic labeling experiments on MnO$_x$/IrO$_x$/GC in an attempt to determine the origin of the oxygen produced by the catalyst. This is made possible by the tendency of oxygen of the IrO$_x$ lattice to participate in the OER mechanism.[85] First, the IrO$_x$ lattice oxygen was partially exchanged with the ^{18}O isotope by performing OER in a 0.1 M KHSO$_4$ solution of "marked water" (H$_2$^{18}O).[85,86] MnO$_x$ was then grown in "regular water" at 1.45 V (a potential just before the OER onset), and OLEMS measurements were performed on this Mn^{16}O$_x$/Ir^{18}O$_x$/GC electrode. By observing changes in the ratio of mass/charge signals 34 and 32,[87] we were able to determine whether the oxygen formed originated from MnO$_x$ (leading to ^{16}O$_2$ and no enrichment in the m/z 34 signal) or Ir^{18}O$_x$ (partially producing ^{18}O–^{16}O and changing the 34/32 ratio). At this point, ^{18}O$_2$ can also be formed; unfortunately, the mass charge ratio of this species (m/z 36) coincides with that of HCl$^+$, a species formed in the ionization chamber, and as such this signal is ambiguous. As can be seen in Figure 11B, the catalyst shows an enrichment of ^{18}O during OER in the first scan. The produced oxygen thus at least partially originates from the subsurface IrO$_x$ layer. The
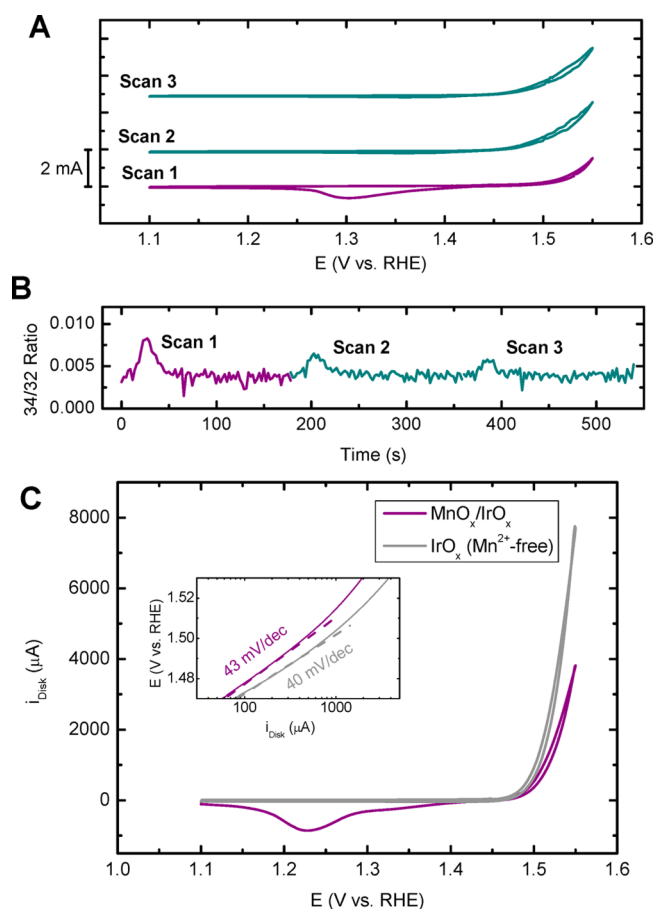

Figure 11. (A and B) OLEMS measurements of an "MnO$_x$/Ir^{18}O$_x$/GC" electrode in 0.5 M KHSO$_4$, 30 mM KCl, and 1.2 mM MnSO$_4$ (pH = 0.87). The isotopic labeling procedure is described in the text. The electrode was scanned three times (A), while monitoring the mass/charge ratio 34/32 (B). Scan rate: 5 mV s^{-1}. (C) CVs of an IrO$_x$/GC rotating disk electrode in 0.5 M Na/HClO$_4$ (pH = 0.85), in a Mn^{2+}-free solution (gray) and in the presence of 0.6 mM Mn(ClO$_4$)$_2$ with a preconditioned MnO$_x$ film before initiating the forward scan at 1.45 V (purple). Inset shows calculated Tafel slopes determined from forward–backward averaged disk currents. Scan rate: 10 mV s^{-1}; rotation rate: 1500 rpm. All solutions are saturated with Ar.

OLEMS experiments were conducted in the presence of chloride, which allowed the monitoring and comparison of MnO$_x$ film growth, as well as ensuring that the experimental conditions were as close as possible to previous OLEMS experiments. In scans 2 and 3, we can see a current increase attributable to increased CER after MnO$_x$ reductive dissolution, in agreement with results from Figure 7. Figure 11C shows OER measurements in a Cl$^-$-free solution of an IrO$_x$/GC catalyst with a pregrown MnO$_x$ film, compared to the same catalyst in a Mn^{2+}-free solution. A nonadsorbing ClO$_4^-$ solution was chosen over HSO$_4^-$ in this experiment since it led to higher OER rates and faster MnO$_x$ growth. The two curves arguably have almost identical onset potentials and very similar Tafel slopes (40 versus 43 mV/dec for IrO$_x$ and MnO$_x$/IrO$_x$, respectively). Both experiments shown in Figure 11 give strong evidence for the conclusion that the MnO$_x$ film itself is inactive for OER, and the OER activity stems from the IrO$_x$ underneath the MnO$_x$ film.

Scheme 1. Sketch of the IrO$_x$/GC Catalyst (A), Deposition Structure of MnOx Deposition on MnO$_x$/IrO$_x$/GC (B),^{a} and a Side-View (C) Showing the Isotopic Labeling Experiment in Figure 11A and B^b
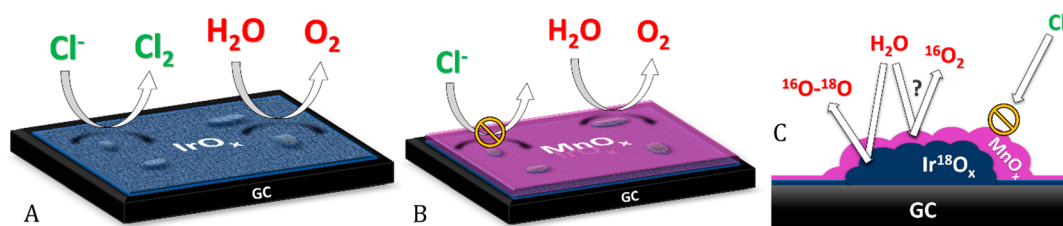
^{a}The MnO$_x$ forms a porous, amorphous network on top of the IrO$_x$ layer, blocking CER by preventing Cl$^-$ from reaching the IrO$_x$ underneath.
^{b}Participation of sub-surface IrO$_x$ in OER is apparent from detection of the enriched m/z 34 signal.

3.5. General Discussion on the Origin of the OER/CER Selectivity. From the above results, we conclude that a MnO$_x$ film facilitates the selective formation of O$_2$ over Cl$_2$, in agreement with previous literature.[39,40] However, contrary to what was previously assumed (at least implicitly), our results show that MnO$_x$ is not actually a catalytically active phase. This conclusion is in fact in agreement with previous literature: MnO$_x$ is generally not very active for OER in strongly acidic media (pH < 1) and certainly cannot be expected to show significant activity within the potential window employed in this work.[37,44,50,88,89] From the OLEMS results, it is clear that MnO$_x$/GC in the absence of IrO$_x$ is not active for either CER or OER at pH ∼0.9, even at high potentials of 1.8 V (Figure S11). Combined with the XPS measurements that indicate very little electronic interaction between MnO$_x$ and IrO$_x$, it is therefore highly unlikely that MnO$_x$ "takes over" OER and CER catalysis from IrO$_x$ when it is deposited. Another feature that strongly disfavors MnO$_x$ being the active catalyst is the OER ability seen in Figure 11C. The MnO$_x$/IrO$_x$/GC electrode displayed an OER current of nearly 5 mA·cm^{-2} (electrode area 0.196 cm^2) at an overpotential of 300 mV, which is at least 3 orders of magnitude higher than even the most optimal performing MnO$_x$ catalysts in alkaline media.[62] The OER current also has a Tafel slope of ∼43 mV/dec, which is very close to 40 mV/dec, the OER Tafel slope of the unmodified IrO$_x$ catalyst. We note that a Tafel slope of less than 60 mV/dec has never been reported for OER on MnO$_x$ at any pH. Finally, OLEMS experiments with isotopically labeled IrO$_x$ (Figure 11A and B, first scan) show that the IrO$_x$ partakes in OER, despite the existence of a MnO$_x$ layer.

Instead of MnO$_x$ being an exceptional catalyst that breaks the apparent scaling between CER and OER, we suggest that the catalytically inert MnO$_x$ functions as a porous overlayer that disfavors the transport of chloride ions, as was also proposed by Bennet.[39] Previous literature suggests that MnO$_x$ deposited at a constant anodic potential usually forms γ-MnO$_2$ (Nsutite) or δ-MnO$_2$ (Birnessite) motifs, where formation of δ-MnO$_2$ seems preferred over γ-MnO$_2$ in the case where Mn^{2+} concentration is in the mM range.[71-73,90-92] The δ and γ polymorphs are both nanoporous and readily intercalate water and cations. From Cl 2p XPS measurements (Figure S20), we detected the presence of an alkali-metal chloride in the IrO$_x$/GC electrode, which can be ascribed to NaCl trapped within the mesoporous IrO$_x$ clusters. By contrast, MnO$_x$/GC displayed no Cl 2p features (despite being grown in a Cl$^-$-containing solution) and neither did MnO$_x$/IrO$_x$/GC, which we interpret as chloride being unable to penetrate the MnO$_x$ film. Furthermore, in the OLEMS results in Figure 7, the O$_2$ signal of scan 1 shows strong tailing, persisting for nearly 100 s

after starting the experiment, which translates to O$_2$ detected down to 1.15 V in the backward scan. We ascribe this effect to O$_2$ trapped in the MnO$_x$ porous structure, which is liberated upon MnO$_x$ dissolution.

Scheme 1 sketches the origin of the observed selectivity behavior with MnO$_x$ deposition (Scheme 1). Starting from the "bare" IrO$_x$ film, initial MnO$_x$ deposition (0 < Q$_{MnO_x}$ < 2 mC) is accompanied by a mild and approximately proportional decrease in OER and CER activity (Figure 3 and Figure 4), implying that at these low coverages both reactions are hindered. The corresponding Tafel plots extracted from the ring currents (Figure 5 and Figure S8) show that the CER slopes retain a value of ∼40 mV/dec, but are shifted gradually upward to higher potentials. A similar effect during the study of CER was reported before by Mozota and Conway[93] and would imply a decrease in the number of active sites with an unchanging reaction mechanism. From electron microscopy micrographs, the MnO$_x$ forms a porous network of amorphous sheets. The dramatic selectivity shift at Q$_{MnO_x}$ > 2 mC then presumably arises when the growing MnO$_x$ sheets start to intertwine and fully cover the IrO$_x$ electrode. MnO$_x$ deposition at this stage seems to solely inhibit CER, whereas OER remains relatively unaffected, suggesting that at this point the film growth is intrinsically different from its initial deposition stage.

When "fully grown", the amorphous MnO$_x$ film still seems to allow transport of H$_2$O, H$^+$, and O$_2$ between IrO$_x$ and the electrolyte. The decreased selectivity versus CER can thus be explained on the basis of concentration overpotentials, in line with recent reports on electrocatalysis at "buried interfaces" by Takanabe et al.[94] and Esposito et al.[95,96] The slow transport of chloride through the MnO$_x$ phase means that near the buried IrO$_x$ interface both the chloride diffusion coefficient and concentration gradient are lowered. This leads to a significant increase of the diffusion layer thickness and an effective increase in the CER overpotential. We further verified the anion-deflecting behavior of MnO$_x$ by performing OER using a MnO$_x$/IrO$_x$/GC catalyst in the presence of bromide ions (Figure S22). In a fashion analogous to Section 3.1, we used the Pt ring as a probe for bromine reduction. We found that the blocking of the bromine evolution reaction is strongly coupled to the presence of the MnO$_x$ film. Lastly, the effect of MnO$_x$ deposition on CER selectivity was verified using a Pt disk electrode as CER catalyst (Figure S23). A MnO$_x$/Pt electrode evolved insignificant amounts of Cl$_2$, whereas the OER onset could be seen near 1.7 V, which is reminiscent of the previously reported OER onset on bare Pt.[97]

IrO$_x$ was also present in the MnO$_x$-based seawater anodes by Hashimoto et al., for which thick heterometal-doped MnO$_x$

coatings were grown on Ti-supported IrO_x (IrO_x/Ti). The IrO_x was added with the intention of preventing the formation of insulating TiO_2 during electrode operation. We believe the OER-selective $Mn_yM_{(1-y)}O_x$/IrO_x/Ti anodes operate in a similar fashion to our MnO_x/IrO_x/GC catalyst under study and that the IrO_x layer may have been crucial for the relatively low polarization resistance during the galvanostatic experiments. The OER selectivity effect of different dopants may have been due to modified MnO_x film stability or morphology under the strongly oxidizing operating conditions.

Application of selective blockage of chloride in seawater electrolysis was recently demonstrated by Ravichandran et al.[98] An analogous case of selectivity induced by a catalytically inert film is likely at hand in the industrial chlorate process, where $Cr(OH)_3$-coated cathodes are used for selective hydrogen evolution.[13,99,100] The H_2-selectivity of the chromium film has been suggested to stem from the selective blocking of dissolved ClO^- anions and oxygen. Interestingly, MnO_x has been recently suggested as a promising alternative to the use of Cr(VI) for the selective hydrogen evolution.[101]

4. CONCLUSION

In this work, we have investigated the unusual OER over CER selectivity of MnO_x-based anodes in the context of hydrogen production from acidic saline water electrolysis. Deposition of a thin MnO_x film onto glassy carbon-supported IrO_x moderately decreases the catalytic activity and strongly shifts the product selectivity from Cl_2 toward O_2, once a critical MnO_x film charge Q_{MnO_x} of approximately 2 mC (10 mC cm^{-2}) is reached. The MnO_x deposit is catalytically inactive and instead seems to function as a diffusion barrier that prevents Cl^- from reacting on the IrO_x catalyst underneath, while still facilitating the transport of water, protons, and O_2 between IrO_x and the electrolyte, necessary for OER activity. The results of this work fit in an emerging trend of using diffusion barriers to affect selectivity. This may be a promising approach in practical brine electrolysis, in contrast to finding an OER catalyst that breaks the intrinsic scaling between selectivity and activity.

■ ASSOCIATED CONTENT

ⓢ Supporting Information

The Supporting Information is available free of charge on the ACS Publications website at DOI: 10.1021/jacs.8b05382.

> Detailed information regarding used chemicals and experimental procedures; supplementary electrochemical and structural data (PDF)

■ AUTHOR INFORMATION

Corresponding Author
*m.koper@lic.leidenuniv.nl

ORCID ⓞ
Marc T. M. Koper: 0000-0001-6777-4594

Notes
The authors declare no competing financial interest.

■ ACKNOWLEDGMENTS

■ REFERENCES

(1) Lewis, N. S. *Science* **2007**, *315*, 798−801.
(2) Bockris, J.; Veziroğlu, T. N. *Int. J. Hydrogen Energy* **1983**, *8*, 323−340.
(3) Bockris, J. *Science* **1972**, *176*, 1323−1323.
(4) Webber, M. E. *Environ. Res. Lett.* **2007**, *2*, 034007.
(5) Suen, N.-T.; Hung, S.-F.; Quan, Q.; Zhang, N.; Xu, Y.-J.; Chen, H. M. *Chem. Soc. Rev.* **2017**, *46*, 337−365.
(6) McCrory, C. C. L.; Jung, S.; Peters, J. C.; Jaramillo, T. F. *J. Am. Chem. Soc.* **2013**, *135*, 16977−16987.
(7) Man, I. C.; Su, H. Y.; Calle-Vallejo, F.; Hansen, H. A.; Martínez, J. I.; Inoglu, N. G.; Kitchin, J.; Jaramillo, T. F.; Nørskov, J. K.; Rossmeisl, J. *ChemCatChem* **2011**, *3*, 1159−1165.
(8) Dionigi, F.; Reier, T.; Pawolek, Z.; Gliech, M.; Strasser, P. *ChemSusChem* **2016**, *9*, 962−972.
(9) Fukuzumi, S.; Lee, Y.-M.; Nam, W. *ChemSusChem* **2017**, *10*, 4264−4276.
(10) World Chlorine Counsil. "Sustainable Progress", downloaded from https://worldchlorine.org/wp-content/uploads/2017/10/WCC_Sustainable-Progress_Version-3-2017_web.pdf on 28−06−2018; 2017.
(11) Euro Chlor. Chlorine Industry Review 2016−2017, downloaded from http://fr.zone-secure.net/13451/398525 on 09−04−2018; 2017.
(12) Trasatti, S. *Electrochim. Acta* **1987**, *32*, 369−382.
(13) Karlsson, R. K. B.; Cornell, A. *Chem. Rev.* **2016**, *116*, 2982−3028.
(14) Schmachtel, S.; Toiminen, M.; Kontturi, K.; Forsén, O.; Barker, M. H. *J. Appl. Electrochem.* **2009**, *39*, 1835−1848.
(15) Oliveira, F. H.; Osugi, M. E.; Paschoal, F. M. M.; Profeti, D.; Olivi, P.; Zanoni, M. V. B. *J. Appl. Electrochem.* **2007**, *37*, 583−592.
(16) Hu, J. M.; Zhang, J. Q.; Cao, C. N. *Int. J. Hydrogen Energy* **2004**, *29*, 791−797.
(17) Koper, M. T. M. *J. Electroanal. Chem.* **2011**, *660*, 254−260.
(18) Burke, L. D.; O'Neill, J. F. *J. Electroanal. Chem. Interfacial Electrochem.* **1979**, *101*, 341−349.
(19) Consonni, V.; Trasatti, S.; Pollak, F.; O'Grady, W. E. *J. Electroanal. Chem. Interfacial Electrochem.* **1987**, *228*, 393−406.
(20) Trasatti, S. *Electrochim. Acta* **1984**, *29*, 1503−1512.
(21) Hansen, H. A.; Man, I. C.; Studt, F.; Abild-Pedersen, F.; Bligaard, T.; Rossmeisl, J. *Phys. Chem. Chem. Phys.* **2010**, *12*, 283−290.
(22) Exner, K. S.; Anton, J.; Jacob, T.; Over, H. *Electrochim. Acta* **2014**, *120*, 460−466.
(23) Exner, K. S.; Anton, J.; Jacob, T.; Over, H. *Angew. Chem., Int. Ed.* **2016**, *55*, 7501−7504.
(24) Martelli, G. N.; Ornelas, R.; Faita, G. *Electrochim. Acta* **1994**, *39*, 1551−1558.
(25) Cherevko, S.; Zeradjanin, A. R.; Topalov, A. A.; Kulyk, N.; Katsounaros, I.; Mayrhofer, K. J. J. *ChemCatChem* **2014**, *6*, 2219−2223.
(26) Topalov, A. A.; Katsounaros, I.; Auinger, M.; Cherevko, S.; Meier, J. C.; Klemm, S. O.; Mayrhofer, K. J. J. *Angew. Chem., Int. Ed.* **2012**, *51*, 12613−12615.
(27) Danilovic, N.; Subbaraman, R.; Chang, K.-C.; Chang, S. H.; Kang, Y. J.; Snyder, J.; Paulikas, A. P.; Strmcnik, D.; Kim, Y.-T.; Myers, D.; Stamenkovic, V. R.; Markovic, N. M. *J. Phys. Chem. Lett.* **2014**, *5*, 2474−2478.
(28) Reier, T.; Pawolek, Z.; Cherevko, S.; Bruns, M.; Jones, T.; Teschner, D.; Selve, S.; Bergmann, A.; Nong, H. N.; Schlögl, R.; Mayrhofer, K. J. J.; Strasser, P. *J. Am. Chem. Soc.* **2015**, *137*, 13031−13040.
(29) Frydendal, R.; Paoli, E. A.; Chorkendorff, I.; Rossmeisl, J.; Stephens, I. E. L. *Adv. Energy Mater.* **2015**, *5*, 1500991.
(30) Comninellis, C.; Vercesi, G. P. *J. Appl. Electrochem.* **1991**, *21*, 335−345.

(31) Panić, V. V.; Dekanski, A. B.; Mišković-Stanković, V. B.; Milonjić, S. K.; Nikolić, B. Ž. *J. Electroanal. Chem.* **2005**, *579*, 67−76.

(32) Chen, S.; Zheng, Y.; Wang, S.; Chen, X. *Chem. Eng. J.* **2011**, *172*, 47−51.

(33) Beer, H. B. *J. Electrochem. Soc.* **1980**, *127*, C303−C307.

(34) Trasatti, S. *Electrochim. Acta* **2000**, *45*, 2377−2385.

(35) Najafpour, M. M.; Renger, G.; Hołyńska, M.; Moghaddam, A. N.; Aro, E.-M.; Carpentier, R.; Nishihara, H.; Eaton-Rye, J. J.; Shen, J.-R.; Allakhverdiev, S. I. *Chem. Rev.* **2016**, *116*, 2886−2936.

(36) Hunter, B. M.; Gray, H. B.; Müller, A. M. *Chem. Rev.* **2016**, *116*, 14120−14136.

(37) Takashima, T.; Hashimoto, K.; Nakamura, R. *J. Am. Chem. Soc.* **2012**, *134*, 1519−1527.

(38) Gorlin, Y.; Jaramillo, T. F. *J. Am. Chem. Soc.* **2010**, *132*, 13612−13614.

(39) Bennett, J. *Int. J. Hydrogen Energy* **1980**, *5*, 401−408.

(40) Fujimura, K.; Izumiya, K.; Kawashima, A.; Akiyama, E.; Habazaki, H.; Kumagai, N.; Hashimoto, K. *J. Appl. Electrochem.* **1999**, *29*, 765−771.

(41) Habazaki, H.; Matsui, T.; Kawashima, A.; Asami, K.; Kumagai, N.; Hashimoto, K. *Scr. Mater.* **2001**, *44*, 1659−1662.

(42) Abdel Ghany, N. A.; Kumagai, N.; Meguro, S.; Asami, K.; Hashimoto, K. *Electrochim. Acta* **2002**, *48*, 21−28.

(43) Kato, Z.; Bhattarai, J.; Kumagai, N.; Izumiya, K.; Hashimoto, K. *Appl. Surf. Sci.* **2011**, *257*, 8230−8236.

(44) Huynh, M.; Bediako, D. K.; Nocera, D. G. *J. Am. Chem. Soc.* **2014**, *136*, 6002−6010.

(45) Takeno, N. *Natl. Inst. Adv. Ind. Sci. Technol. Tokyo* **2005**, No. 419, 1−285.

(46) Fan, K.; Chen, H.; Ji, Y.; Huang, H.; Claesson, P. M.; Daniel, Q.; Philippe, B.; Rensmo, H.; Li, F.; Luo, Y.; Sun, L. *Nat. Commun.* **2016**, *7*, 11981.

(47) Trześniewski, B. J.; Diaz-Morales, O.; Vermaas, D. A.; Longo, A.; Bras, W.; Koper, M. T. M.; Smith, W. A. *J. Am. Chem. Soc.* **2015**, *137*, 15112−15121.

(48) Yang, X.; Wang, C.-J.; Hou, C.-C.; Fu, W.-F.; Chen, Y. *ACS Sustainable Chem. Eng.* **2018**, *6*, 2893−2897.

(49) Burke, M. S.; Kast, M. G.; Trotochaud, L.; Smith, A. M.; Boettcher, S. W. *J. Am. Chem. Soc.* **2015**, *137*, 3638−3648.

(50) Pokhrel, R.; Goetz, M. K.; Shaner, S. E.; Wu, X.; Stahl, S. S. *J. Am. Chem. Soc.* **2015**, *137*, 8384−8387.

(51) Vos, J. G.; Koper, M. T. M. *J. Electroanal. Chem.* **2018**, *819*, 260−268.

(52) Najafpour, M. M.; Khoshkam, M.; Jafarian Sedigh, D.; Zahraei, A.; Kompany-Zareh, M. *New J. Chem.* **2015**, *39*, 2547−2550.

(53) Nijjer, S.; Thonstad, J.; Haarberg, G. M. *Electrochim. Acta* **2000**, *46*, 395−399.

(54) Filipe, O.; Brett, C. M. A. *Talanta* **2003**, *61*, 643−650.

(55) Paul, R. L.; Cartwright, A. *J. Electroanal. Chem. Interfacial Electrochem.* **1986**, *201*, 123−131.

(56) Rogulski, Z.; Siwek, H.; Paleska, I.; Czerwiński, A. *J. Electroanal. Chem.* **2003**, *543*, 175−185.

(57) Guerrini, E.; Consonni, V.; Trasatti, S. *J. Solid State Electrochem.* **2005**, *9*, 320−329.

(58) Scharifker, B.; Hills, G. *Electrochim. Acta* **1983**, *28*, 879−889.

(59) Mostany, J.; Scharifker, B. In *Encyclopedia of Electrochemistry*; Bard, A. J.; Stratmann, M.; Calvo, E. J., Eds.; Wiley-VCH Verlag GmbH & Co. KGaA: Weinheim, Germany, 2007; Vol. 2, pp 512−540.

(60) Huynh, M.; Bediako, D. K.; Liu, Y.; Nocera, D. G. *J. Phys. Chem. C* **2014**, *118*, 17142−17152.

(61) Sohrabnejad-Eskan, I.; Goryachev, A.; Exner, K. S.; Kibler, L. A.; Hensen, E. J. M.; Hofmann, J. P.; Over, H. *ACS Catal.* **2017**, *7*, 2403−2411.

(62) Huynh, M.; Shi, C.; Billinge, S. J. L.; Nocera, D. G. *J. Am. Chem. Soc.* **2015**, *137*, 14887−14904.

(63) Gorlin, Y.; Chung, C.-J.; Benck, J. D.; Nordlund, D.; Seitz, L. C.; Weng, T.-C.; Sokaras, D.; Clemens, B. M.; Jaramillo, T. F. *J. Am. Chem. Soc.* **2014**, *136*, 4920−4926.

(64) Seitz, L. C.; Hersbach, T. J. P.; Nordlund, D.; Jaramillo, T. F. *J. Phys. Chem. Lett.* **2015**, *6*, 4178−4183.

(65) Ramírez, A.; Hillebrand, P.; Stellmach, D.; May, M. M.; Bogdanoff, P.; Fiechter, S. *J. Phys. Chem. C* **2014**, *118*, 14073−14081.

(66) Zhao, Y.; Hernandez-Pagan, E. A.; Vargas-Barbosa, N. M.; Dysart, J. L.; Mallouk, T. E. *J. Phys. Chem. Lett.* **2011**, *2*, 402−406.

(67) Zhao, Y.; Vargas-Barbosa, N. M.; Hernandez-Pagan, E. A.; Mallouk, T. E. *Small* **2011**, *7*, 2087−2093.

(68) Nakagawa, T.; Beasley, C. A.; Murray, R. W. *J. Phys. Chem. C* **2009**, *113*, 12958−12961.

(69) Yagi, M.; Tomita, E.; Kuwabara, T. *J. Electroanal. Chem.* **2005**, *579*, 83−88.

(70) Cheney, M. A.; Bhowmik, P. K.; Moriuchi, S.; Villalobos, M.; Qian, S.; Joo, S. W. *J. Nanomater.* **2008**, *2008*, 1−9.

(71) Nakayama, M.; Kanaya, T.; Lee, J.-W.; Popov, B. N. *J. Power Sources* **2008**, *179*, 361−366.

(72) Post, J. E. *Proc. Natl. Acad. Sci. U. S. A.* **1999**, *96*, 3447−3454.

(73) Zaharieva, I.; Chernev, P.; Risch, M.; Klingan, K.; Kohlhoff, M.; Fischer, A.; Dau, H. *Energy Environ. Sci.* **2012**, *5*, 7081−7089.

(74) Gorlin, Y.; Lassalle-Kaiser, B.; Benck, J. D.; Gul, S.; Webb, S. M.; Yachandra, V. K.; Yano, J.; Jaramillo, T. F. *J. Am. Chem. Soc.* **2013**, *135*, 8525−8534.

(75) Huynh, M.; Bediako, D. K.; Liu, Y.; Nocera, D. G. *J. Phys. Chem. C* **2014**, *118*, 17142−17152.

(76) Michell, D.; Rand, D. A. J.; Woods, R. *J. Electroanal. Chem. Interfacial Electrochem.* **1977**, *84*, 117−126.

(77) Ortel, E.; Reier, T.; Strasser, P.; Kraehnert, R. *Chem. Mater.* **2011**, *23*, 3201−3209.

(78) Abbott, D. F.; Lebedev, D.; Waltar, K.; Povia, M.; Nachtegaal, M.; Fabbri, E.; Copéret, C.; Schmidt, T. J. *Chem. Mater.* **2016**, *28*, 6591−6604.

(79) Massué, C.; Pfeifer, V.; van Gastel, M.; Noack, J.; Algara-Siller, G.; Cap, S.; Schlögl, R. *ChemSusChem* **2017**, *10*, 4786−4798.

(80) Kötz, R.; Neff, H.; Stucki, S. *J. Electrochem. Soc.* **1984**, *131*, 72.

(81) Pfeifer, V.; Jones, T. E.; Velasco Vélez, J. J.; Massué, C.; Greiner, M. T.; Arrigo, R.; Teschner, D.; Girgsdies, F.; Scherzer, M.; Allan, J.; Hashagen, M.; Weinberg, G.; Piccinin, S.; Hävecker, M.; Knop-Gericke, A.; Schlögl, R. *Phys. Chem. Chem. Phys.* **2016**, *18*, 2292−2296.

(82) Junta, J. L.; Hochella, M. F. *Geochim. Cosmochim. Acta* **1994**, *58*, 4985−4999.

(83) Cerrato, J. M.; Hochella, M. F.; Knocke, W. R.; Dietrich, A. M.; Cromer, T. F. *Environ. Sci. Technol.* **2010**, *44*, 5881−5886.

(84) Smith, R. D. L.; Sporinova, B.; Fagan, R. D.; Trudel, S.; Berlinguette, C. P. *Chem. Mater.* **2014**, *26*, 1654−1659.

(85) Fierro, S.; Nagel, T.; Baltruschat, H.; Comninellis, C. *Electrochem. Commun.* **2007**, *9*, 1969−1974.

(86) Grimaud, A.; Diaz-Morales, O.; Han, B.; Hong, W. T.; Lee, Y.; Giordano, L.; Stoerzinger, K. A.; Koper, M. T. M.; Shao-Horn, Y. *Nat. Chem.* **2017**, *9*, 457−465.

(87) Stoerzinger, K. A.; Diaz-Morales, O.; Kolb, M.; Rao, R. R.; Frydendal, R.; Qiao, L.; Wang, X. R.; Halck, N. B.; Rossmeisl, J.; Hansen, H. A.; Vegge, T.; Stephens, I. E. L.; Koper, M. T. M.; Shao-Horn, Y. *ACS Energy Lett.* **2017**, *2*, 876−881.

(88) Morita, M.; Iwakura, C.; Tamura, H. *Electrochim. Acta* **1979**, *24*, 357−362.

(89) Morita, M.; Iwakura, C.; Tamura, H. *Electrochim. Acta* **1977**, *22*, 325−328.

(90) Nakayama, M.; Fukuda, M.; Konishi, S.; Tonosaki, T. *J. Mater. Res.* **2006**, *21*, 3152−3160.

(91) Rodrigues, S.; Shukla, a K.; Munichandraiah, N. *J. Appl. Electrochem.* **1998**, *28*, 1235−1241.

(92) Biswal, A.; Chandra Tripathy, B.; Sanjay, K.; Subbaiah, T.; Minakshi, M. *RSC Adv.* **2015**, *5*, 58255−58283.

(93) Mozota, J.; Conway, B. E. *J. Electrochem. Soc.* **1981**, *128*, 2142−2149.

(94) Garcia-Esparza, A. T.; Shinagawa, T.; Ould-Chikh, S.; Qureshi, M.; Peng, X.; Wei, N.; Anjum, D. H.; Clo, A.; Weng, T.-C.; Nordlund,

D.; Sokaras, D.; Kubota, J.; Domen, K.; Takanabe, K. *Angew. Chem., Int. Ed.* **2017**, *56*, 5780−5784.

(95) Labrador, N. Y.; Songcuan, E. L.; De Silva, C.; Chen, H.; Kurdziel, S. J.; Ramachandran, R. K.; Detavernier, C.; Esposito, D. V. *ACS Catal.* **2018**, *8*, 1767−1778.

(96) Esposito, D. V. *ACS Catal.* **2018**, *8*, 457−465.

(97) Damjanovic, A.; Dey, A.; Bockris, J. *Electrochim. Acta* **1966**, *11*, 791−814.

(98) Balaji, R.; Kannan, B. S.; Lakshmi, J.; Senthil, N.; Vasudevan, S.; Sozhan, G.; Shukla, A. K.; Ravichandran, S. *Electrochem. Commun.* **2009**, *11*, 1700−1702.

(99) Lindbergh, G.; Simonsson, D. *J. Electrochem. Soc.* **1990**, *137*, 3094.

(100) Endrődi, B.; Simic, N.; Wildlock, M.; Cornell, A. *Electrochim. Acta* **2017**, *234*, 108−122.

(101) Endrődi, B.; Sandin, S.; Smulders, V.; Simic, N.; Wildlock, M.; Mul, G.; Mei, B. T.; Cornell, A. *J. Cleaner Prod.* **2018**, *182*, 529−537.